

# A Deep learning framework for Single sided sound speed inversion in medical ultrasound

Micha Feigin, Daniel Freedman, Brian W. Anthony

**Abstract**—Ultrasound elastography is gaining traction as an accessible and useful diagnostic tool for such things as cancer detection and differentiation as well as liver and thyroid disease diagnostics. Unfortunately, state of the art acoustic radiation force techniques are limited to high end ultrasound hardware due to high power requirements, are extremely sensitive to patient and sonographer motion and generally suffer from low frame rates.

Researchers have shown that pressure wave velocity possesses similar diagnostic abilities to shear wave velocity. Using pressure waves removes the need for generating shear waves, in turn, enabling elasticity based diagnostic techniques on portable and low cost devices. However, current travel time tomography and full waveform inversion techniques for recovering pressure wave velocities, require a full circumferential field of view. Focus based techniques on the other hand provide only localized measurements, and are sensitive to the intermediate medium.

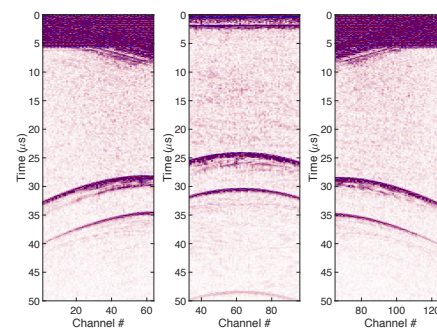
In this paper, we present a single sided sound speed inversion solution using a fully convolutional deep neural network. We show that it is possible to invert for longitudinal sound speed in soft tissue at real time frame rates. For the computation, analysis is performed on channel data information from three diagonal plane waves. This is the first step towards a full waveform solver using a deep learning framework for the elastic and viscoelastic inverse problem.

## I. INTRODUCTION

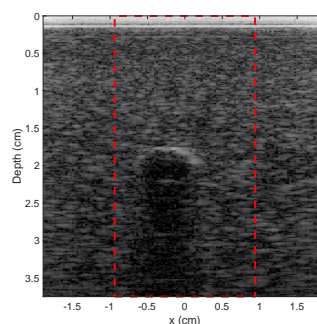
Abnormalities in the mechanical tissue properties, tissue structures, and the spatial arrangement of properties and structures are useful in disease diagnosis in the kidneys [1], [2], thyroid, muscle, breast [3], [4], liver [5], [6], prostate, and other organs. Tracking changes to tissue properties, tissue structure, and spatial distribution of both is useful for monitoring disease progression or response to therapeutic interventions.

Embedded in ultrasound signals is information about the mechanical (and acoustic) properties of the tissue through which the ultrasound waves have propagated or from which ultrasound waves have been reflected. Properties include the longitudinal-wave speed of sound, shear-wave speed of sound, tissue density, attenuation, shear modulus, and bulk modulus. As part of the classical b-mode imaging process however, significant parts of this information are discarded through the application of beam forming (delay and sum focusing) and envelope detection.

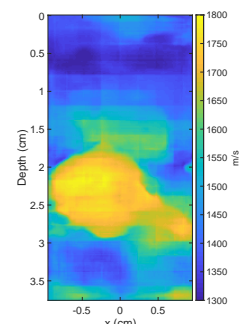
Being able to provide quantitative real time diagnostically relevant measurements and good differentiation properties, especially such that can function on low cost as well as high end devices and volumetric imaging, is highly enticing and can greatly assist the physician workflow. It will improve real



(a) Channel data input



(b) b-mode image



(c) Sound speed output

Fig. 1. Goal: the target of this work is to be able to take raw ultrasound channel data (a) and in addition to the standard b-mode image (b), also produce the corresponding tissue sound speed map (c)

time decision making for experts while at the same time make high level of care more accessible in locations where direct access to experts is limited, such as the developing world and rural areas.

In the past several years, we have seen a burst of interest in the use of AI for improving the physician work flow. From automatic analysis and improvement of medical images to incorporating medical data and physician notes into diagnostics. Large amounts of research go into analyzing image attributes for the purpose of using them as disease biomarkers. Most, if not all, of this research however, focuses on processing the final physician-oriented images rather than raw data or the data collection and image generation pipeline. In general, there has been little to no work using deep learning for the inverse problem applied to raw signals (channel data).

In this work we exploit the information embedded in the raw ultrasound channel data signal. As depicted in Fig 1, we take ultrasound channel data and generate the sound speed map of the tissue. This resulting information is invaluable

M. Feigin and B. W. Anthony are with the Department of Mechanical Engineering, Massachusetts Institute of Technology, Cambridge, MA, USA.

D. Freedman is with Google Research, Haifa, Israel.

both directly for diagnostic purposes, as well as indirectly, for improving image quality. To this end, we harness the power of deep convolutional neural networks.

This work is the first step towards implementing a full waveform solver for recovering more general elastic and viscoelastic tissue parameters using deep learning, and shows the viability of this framework to such applications.

Despite numerous applications of various inverse problem between different image domains, this is the first implementation we are aware of applying a deep learning framework to raw time domain RF type signals. This is also the first solution we are aware of that works toward single sided full waveform inversion in the ultrasound domain, all the more so, on a standard ultrasound probe.

A big advantage of our system is that it can work at real time frame rates, with the current implementation running at over 150fps on a single NVIDIA 1080Ti. It require only a small number of transmits, so can run in parallel to standard imaging.

## II. BACKGROUND AND PRIOR WORK

We divide our discussion of background and prior work into three domains. We start with some background on ultrasound elastography, continue with clinical motivation, and summarize with an overview on deep learning.

### A. Elastography and Full waveform inversion

The currently employed model for ultrasound elastography of soft tissue is that of a linear isotropic elastic material. While this does not account for non-linear effects, it is still useful for diagnostic purposes for most soft tissues, and can be extended to include the viscoelastic based attenuation by employing a complex sound speed.

Under this model, tissue can be described using density and two independent elastic coefficients. Some of the commonly used pairs are Young's modulus ( $E$ ) and Poisson ratio ( $\nu$ ), the bulk modulus ( $K$ ) and shear modulus ( $G$ ), or the two Lamme parameters ( $\lambda$  and  $\mu$ ). Here, the shear modulus and Lamme's second parameter are the same value. Of these, the Young's modulus is often used to describe tissue stiffness, and is the value most closely related to what we intuitively perceive as material stiffness. The complimentary elastic parameter and the density are often assumed to be constant, and dominated by the tissue high water content.

The pressure wave, p-wave (primary wave) or longitudinal wave is an acoustic wave used for ultrasound imaging, and travels at  $1540\text{ m/s}$  on average in soft tissue. The shear wave, s-wave (secondary wave) or transverse wave is measured indirectly in ultrasound elastography, using pressure waves, is much slower, traveling at velocities on the order of  $3\text{ m/s}$  in healthy tissue, up to  $60\text{ m/s}$  in highly pathological tissue. In soft tissue, when working in the linear regime, pressure waves and the two orthogonally polarized shear waves are considered independent, as they only distinctly couple at strong discontinuities.

Ultrasound shear wave imaging, is the currently deployed state of the art [7], [8], [9]. Common methods of shear wave

Brest tissue type	# of samples	Young's modulus (kPa) mean $\pm$ STD
Normal fat	71	$3.25 \pm 0.91$
Normal fibroglandular tissue	26	$3.24 \pm 0.61$
Fibroadenoma	16	$6.41 \pm 2.86$
Low-grade IDC	12	$10.40 \pm 2.60$
ILC	4	$15.62 \pm 2.64$
DCIS	4	$16.38 \pm 1.55$
Fibrocystic disease	4	$17.11 \pm 7.35$
Intermediate-grade IDC	21	$19.99 \pm 4.2$
High-grade IDC	9	$42.52 \pm 12.47$
IMC	1	20.21
Fat necrosis	1	4.45

TABLE I  
YOUNG'S MODULUS AS A DISEASE BIOMARKER FOR VARIOUS BREAST TISSUE TYPES [22], [23]

generation include acoustic radiation force (ARFI) [8] and supersonic shear wave [10], [11]. A mechanical shear wave is generated in the tissue and its propagation velocity is tracked using pressure waves. Some devices return the actual measured shear wave velocity, while others approximate the Young's modulus by assuming that the Poisson ratio and mass density are fixed [12], [13] and using the relation

$$E = 2G(1 + \nu) \approx 3\rho V_s^2.$$

These methods however are limited to high end devices due in high power and probe requirements. They also generally suffer from low frame rates, long settling times and high sensitivity to sonographer and subject motion.

Active research is being conducted on tomographic ultrasound imaging for travel time tomography and full waveform inversion, mostly focused on breast [14], [15], [16], [17], [18], [19], and musculoskeletal [20], [21] imaging, both showing promising prospects. Current implementation in tissue however require a full circumferential field of view, limiting them to small body parts. Both are also extremely computationally expensive and sensitive to noise and choice of initial conditions. Single sided techniques are in use in the seismic domain, but usually require operator intervention for good results.

### B. Clinical motivation

Short of attaining fully automated diagnostics, the next best holy grail is to solve the inverse problem of measuring physical tissue properties. Focus is given to properties that can be used directly by the physician as reliable disease biomarkers. Achieving that end in an accessible and easily undertaken way can greatly improve the physician workflow as well as make quality health care much more accessible.

Current research is mostly split in two directions, shear wave elastography and ultrasound tomography, both travel time tomography and full waveform inversion. Table I presents Young's modulus values for several healthy and pathological breast tissues as given by [22], [23]. As can be seen, this is a good indicative value for detecting and differentiating pathological tissue.

Researchers have also shown that pressure wave sound speed has similar diagnostic ability to shear wave imaging [24], [25], [26], [19], [27], [28]. Some of these results taken on breast tissue are presented in table II (extracted from [26]).

Brest tissue type	Sound speed (m/s)
Normal fat	1442 ± 9
Breast parenchyma	1487 ± 21
Benign breast lesions	1513 ± 27
Malignant breast lesions	1548 ± 17

TABLE II  
LONGITUDINAL SOUND SPEED AS A DISEASE BIOMARKER FOR VARIOUS  
BREAST TISSUE TYPES [26]

Using longitudinal speed of sound as a substitute for transverse speed of sounds presents several potential advantages. For starters, longitudinal waves travel significantly faster in tissue than transverse waves, allowing for much higher frame rates. Secondly, transverse waves cannot be detected directly on the probe, due to their strong attenuation in tissue along with low sensitivity of the Piezo sensors to transverse motion. As a result they are only imaged indirectly by their effect on longitudinal waves. The particle motion that is detected is on the order of 10 microns, resulting with measurements that are highly sensitive to probe and subject motion. The amount of energy required to generate shear waves using acoustic radiation force is also high, requiring high powered devices, limiting this technology to high end ultrasound machines, while at the same time again limiting frame rates due to FDA limitations on transmission power and long settling times.

As a clinical imaging modality, ultrasound is differentiated from modalities such as computerized X-ray tomography (CT) and Magnetic resonance imaging (MRI) in that it uses non-ionizing radiation, is mobile, and has a significantly lower purchase and operating costs than most other medical imaging alternatives. The mode of operation is significantly different, where an interactive exploratory approach is taken. The operator can move the probe around, vary applied pressure and adapt to findings in real time, making real time quantitative diagnosis techniques that much more important. On the down side, different tissue types are not differentiated in the images, requiring more experience to interpret the images.

### C. Deep learning

The astounding success of Deep Learning in fields including computer vision, speech recognition, and natural language processing is by now widely known. Neural networks have achieved state of the art results on many benchmarks within each of these fields. In most cases, the networks in question are relatively deep (tens or hundreds of layers), and are trained by stochastic gradient descent or related techniques, as implemented by the standard backpropagation algorithm.

Deep Learning has also achieved great success in medical imaging on standard computer vision tasks, such as classification [29], detection [30], and segmentation [31]. However, it is only more recently that Deep Learning has been applied to problems in sensing and image reconstruction. The growing popularity of this trend is exemplified by the recent special issue (June 2018) of TMI which was devoted to this topic. The issue contained many papers related to both CT and MRI. Within the realm of CT, a variety of topics were examined, including artifact reduction [32], denoising [33], [34], and sparse-view [35], [36] and low-dose [37], [38] reconstruction.

Papers on MRI tended to focus on Deep Learning approaches to compressive sensing [39], [40], [41]. Deep Learning has also been applied, though not quite as widely, to PET [42], [43] and Photoacoustic Tomography [44], [45]. Furthermore, we note that in the broader signal processing community, work has been devoted to applying Deep Learning techniques to general reconstruction problems, such as compressive sensing [46] and phase retrieval [47].

Within the field of ultrasound, Deep Learning has been successfully employed in a few areas. Vedula *et al.* [48] train a multi-resolution CNN to generate CT quality images from raw ultrasound measurements. Yoon *et al.* [49] apply Deep Learning to produce B-mode images from a small number of measurements, which can circumvent the heavy computational load imposed by competing compressed sensing algorithms. Tom and Sheet [50] propose a method for generating B-mode images based on generative adversarial networks, which obviates the need for running expensive wave equation solvers. Luchies and Byram [51] apply Deep Learning to the problem of beamforming in ultrasound, for the purpose of minimizing off-axis scattering. Reiter and Bell [52] use a CNN to identify a common type of ultrasound artifact, namely the reflection artifact that arises when a small point-like target is embedded in the middle of an echogenic structure.

Finally, we note that Deep Learning has also been applied in non-reconstruction tasks to ultrasound, including classification [53], [54] and segmentation [55].

## III. SIMULATIONS

Collecting real world ground truth data in quantities sufficient for training a neural network, is practically impossible. This leaves us with the alternative of using simulated data.

For training purposes, we have developed a simplified soft tissue model for organs and lesions. We model tissue as a uniform background with a mix of between one and five randomly selected ellipses, randomly selecting position, size and rotation using a uniform distribution. The sound speed for the background and each of the ellipses is randomly selected with uniform distribution in the range of 1300 *m/s* and 1800 *m/s*. Random speckle is added in the density domain, with a mean mass density of 0.9 *g/cm*<sup>3</sup>, uniformly distributed mass density variations between -3% and +6% and a mean distribution density of 2 reflectors per  $\lambda^2$ . Attenuation is fixed at 0.5 *dB/(MHz · cm)*, or 2.5 *dB/cm* at the center frequency of 5 *MHz*. For the recovered domain we chose the central section, 1.875 *cm* wide by 3.75 *cm* deep. This is guided by coverage limitations due to maximum aperture size combined with showing that we can handle signals arriving from outside the recovered domain.. The setup is depicted in Fig 2.

For a numerical solver we work with is the k-wave toolbox for MATLAB [56], [57]. It presents a compromise that can deal with both discontinuities as well as speckle noise over non-uniform domains, while maintaining decent run times on an NVIDIA GPU.

We model the sensor based on our physical system, a Cephasonics Cicada LX, capable of transmitting on 64 channels at a time. The ultrasound probe is a 1D linear array transmitting at

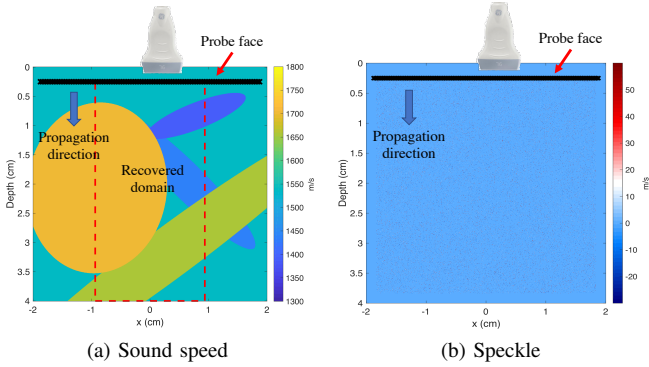


Fig. 2. Simulation setup. Reflecting objects are defined in the sound speed domain (a). Ultrasound speckle is defined in the density domain (b). The probe face is at the top end of the domain, marked by hash marks, and is outside the PML, propagation is towards the bottom. The recovered sound speed domain is marked by a red dashed line in (a).

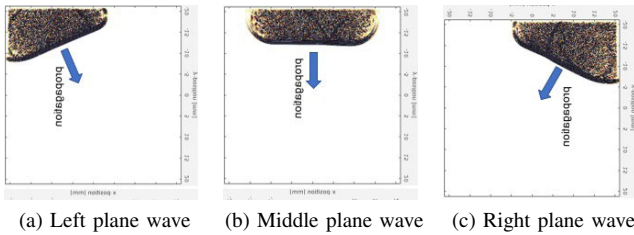


Fig. 3. The diagonal three plane waves generated in k-wave as well as by the real probe. Each plane wave is generated by 64 elements (half the probe), the limit of our current system.

a central frequency of 5 MHz. The probe face is 3.75 cm wide and contains 128 elements. The probe plane is located just outside the PML with four grid points per Piezo element and an extra four grid points for the kerf. The total grid dimension is 4.24 cm by 4.24 cm.

For the transmit pattern we are limited by three parameters, simulation time, network resources and signal to noise ratio (SNR). Both simulation time as well as network run time and resources are controlled by the number of pulses. In this work we look at using either one or three transmit pulses. This hinders us from using the classic scanning focused beam imaging approach. Due to SNR issues, using point source transmits, *i.e.* transmitting from a single element, is also not a good option. As a result, we chose to work with three plane waves. One direct plane wave transmitted from the center of the probe, and two diagonal plane waves from the edges. These plane waves are depicted in Fig 2.

#### IV. NETWORK SETUP

We now describe the structure of our neural network. We wish to map signals to signals, hence we use a type of fully convolutional neural network (FCNN) - that is, there are no fully-connected layers, only convolutional layers, in addition to various non-linear activations. However, most FCNNs assume the input and output sizes are identical, whereas that is not the case in our setup. Therefore, we use striding within the convolutions in order to effectively achieve decimation.

Our base network architecture is depicted in Fig 4, and possesses an “hourglass” structure. In examining Fig 4, note the  $C \times H \times W$  convention is used to describe the size of the layer’s output: that is, number of channel times height times width. The structure is referred to as hourglass due to its shape: in the initial layers (shown in orange in Fig 4), the resolution decreases, *i.e.*  $H$ ,  $W$ , both decrease; while the number of channels increases, from the initial 1, to 32, 64, 128, and finally 512. Thus, the layers get smaller but longer. In the second half of the network (shown in blue in Fig 4), the process is reversed: the resolution increases, while the number of channels goes down, finally reaching a single channel at the output. Thus, the layers get larger but shorter.

We now describe the architecture in greater details, paying attention not just to the convolutional structure but also to the various activations used. On the downsampling path, the first four stages consist of a strided  $3 \times 3$  convolution followed by batch normalization and a Relu operation. Note that the stride used is 2 in the width dimension, which has the effect of downsampling that dimension by a factor of 2. (In fact, the downsampling factor is sometimes not exactly 2; this is due to the nature of the convolutional padding used in the particular layer.) The following three stages consist of an ordinary (non-strided)  $3 \times 3$  convolution followed by batch normalization, Relu and a  $2 \times 2$  maxpool. The latter operation has the effect of reducing the resolution by a factor of 2 in both height and width dimensions (again, approximately, depending on the convolutional padding used). For the upsampling path, each of the first three stages consist of a  $3 \times 3$  convolution followed by batch normalization, Relu and a  $\times 2$  up-sampling. The fourth stage involves a  $3 \times 3$  convolution followed by batch normalization, Relu and linear interpolation. The fifth stage is a  $3 \times 3$  convolution followed by batch normalization, Relu (and no upsampling / interpolation). The final stage is a  $1 \times 1$  convolution, which reduces the number of channels to one, and generates the output.

The base network shown in Fig 4 has the capability of dealing with a single plane-wave. We would like to use a variant of this base network for dealing with three plane-waves. Three different possibilities are depicted in Fig 5. In the “Start Network”, the three plane waves are simply concatenated into a 3-channel image, and the remainder of the base network is identical. In the “Middle Network”, the three plane-waves are each passed into identical subnetworks for the downsampling part of the base network; the results are then concatenated channel-wise, and then remainder of the upsampling part of the base network is the same. In the “End Network”, the same idea is used, but the channel-wise concatenation only happens at the very end, prior to the  $1 \times 1$  convolution. Note that for both Middle and End Networks, weight-sharing in the training phase ensures that each plane-wave is treated identically.

#### V. EXPERIMENTAL RESULTS

Let us now shift our attention to experimental results. We will present results for both synthetic data as well as initial results for real data.

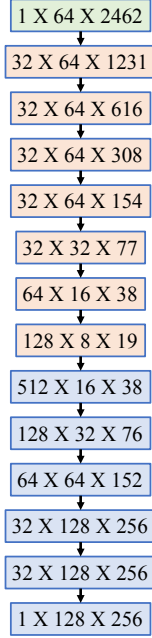


Fig. 4. Base network setup, for handling a single transmitted plane wave signal. The green layer denotes the input layer. Orange layers are the downscaling layers. Blue layers are the upscaling layers.

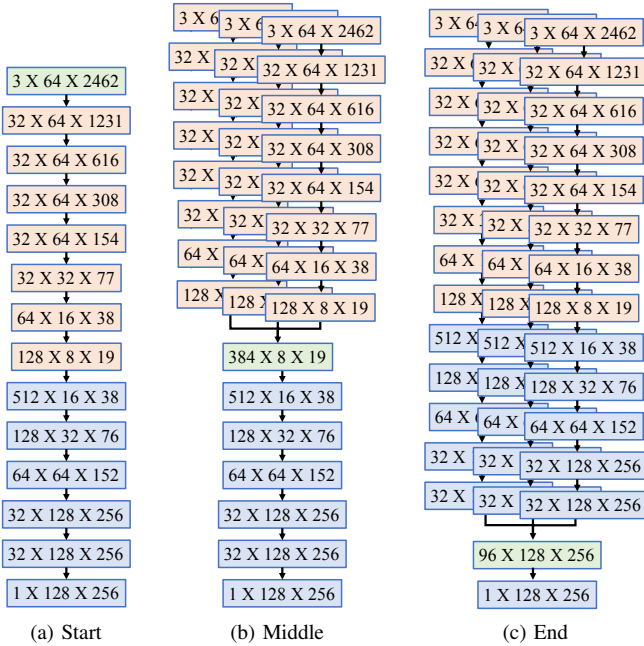
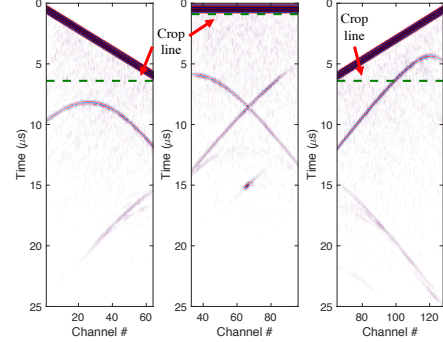


Fig. 5. Network configurations for dealing with the data from multiple plane waves (multiple transmissions). The green layer denotes the data concatenation layer. Orange layers are the downscaling layers. Blue layers are the upscaling layers.



(a) Cropped channel data

Fig. 6. Input channel data is cropped to remove the transmit pulse. Dashed green line shows the crop point for each of the plane waves. This is done to avoid signal saturation.

For the training of the neural network, we used the k-wave toolbox for Matlab to generate 6026 random training samples and 800 test samples as described in Sec III. Before feeding the data into the network, gain correction is applied at a rate of  $0.48 \text{ dB}/\mu\text{s}$  ( $2.5 \text{ dB}/\text{cm}$  at  $1540 \text{ m/s}$ ). The channel data signals are then cropped to remove the transmit pulse, as depicted in Fig 6. This is done to avoid the saturated signal that deteriorates the reconstruction. Our physical system also suffers from electric cross-talk during transmit, corrupting the data in the said range, as seen in Fig. 1a.

Figure 7 presents reconstruction results on several samples from the test data. Recovery works well on larger objects but can miss fine details, as can be seen for example in image 16. Figure 8 shows absolute error values for the samples shown in Fig 7, cropped at  $50 \text{ m/s}$ . Another thing we can see is that there is a slight misalignment at the edges. As a result, although we do show the classic root mean square error (RMSE) values, they do not convey the full story. As RMSE is an  $L_2$  norm, it is sensitive to outliers. Apart for also looking at mean absolute error and the median absolute error, we also look at a modified error value. For each pixel, we take the minimum absolute error within a window with a radius of 5 pixel. Results are presented in table reftab:error.

Available research suggests that for clinically relevant results, measurement accuracy on the order of  $30 \text{ m/s}$  is useful. All results are well within that range, and using error measures that account for outliers at edges, are an order of magnitude better. While more work is required to improve results on real data, we definitely see huge potential with our proposed technology.

Looking at the potential for using multiple inputs, while combining multiple inputs at the first layer, does not improve reconstruction results, both the “middle” and “end” do provide some improvement. However all cases are close to the recovery limit, so we expect more value in terms of stability to noise when dealing with real data.

#### A. Real data

For real data we look at two cases, a polyurethane phantom with an inclusion (Fig 9) and an image of the thyroid (Fig 10).

Network	Train							Test						
	RMSE	$\mu$	$\sigma$	Median	$\mu^*$	$\sigma^*$	Median*	RMSE	$\mu$	$\sigma$	Median	$\mu^*$	$\sigma^*$	Median*
Left	22.4	14.6	17.0	10.6	2.0	4.6	0.18	24.8	16.3	18.7	11.8	2.6	6.0	0.22
Center	23.3	15.1	17.8	10.7	2.5	5.7	0.19	25.2	16.2	19.3	11.4	3.1	7.0	0.24
Right	19.2	12.2	14.8	8.9	1.9	4.1	0.16	22.2	14.4	16.9	10.5	2.3	5.4	0.19
Start	21.8	14.2	16.9	10	2.4	5.4	0.19	24.3	15.6	18.6	11.0	2.9	6.5	0.23
Middle	18.8	11.5	14.9	8.2	2.1	4.3	0.17	20.5	12.5	16.1	8.7	2.6	5.2	0.21
End	18.9	11.9	14.8	8.5	1.6	3.7	0.14	20.8	12.9	16.3	9.0	2.0	5.0	0.16

TABLE III

RECONSTRUCTION ERROR FOR THE TRAIN AND TEST SETS FOR OUR SIX RECOVERY CASES. SINGLE PLANE WAVE RECONSTRUCTION FOR THE THREE PLANE WAVES, AND THREE PLANE WAVE RECONSTRUCTION FOR THE THREE JOINT RECONSTRUCTION NETWORKS. ALL VALUES ARE IN METERS PER SECONDS. RMSE IS THE ABSOLUTE ROOT MEAN SQUARE ERROR.  $\mu$  AND  $\sigma$  ARE THE MEAN AND STANDARD DEVIATION VALUES FOR THE MEAN ABSOLUTE ERROR. MEDIAN IS THE MEDIAN ABSOLUTE ERROR. THE STAR VALUES ARE FOR OUR MODIFIED ERROR VALUES, TAKING THE MINIMUM ABSOLUTE ERROR OVER A WINDOW WITH A RADIUS OF 5 PIXELS.

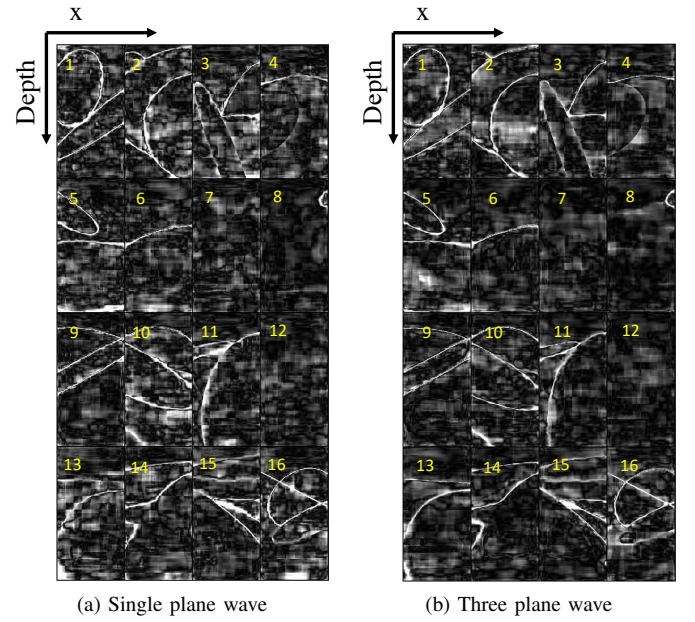
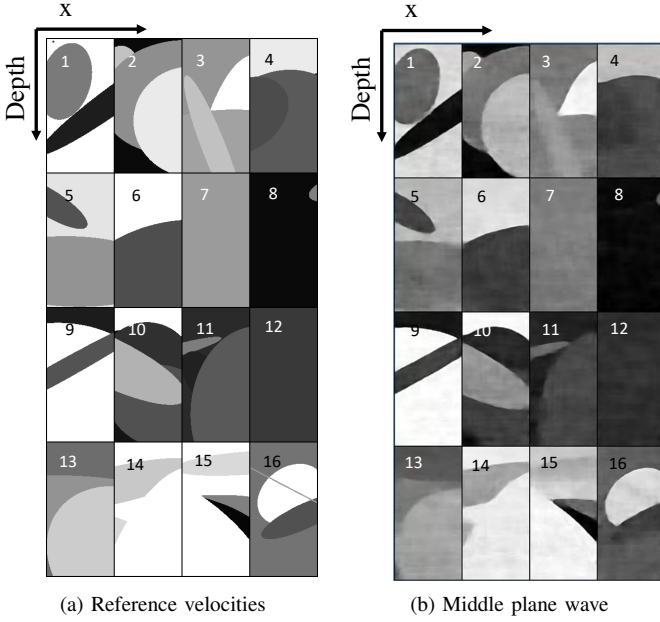


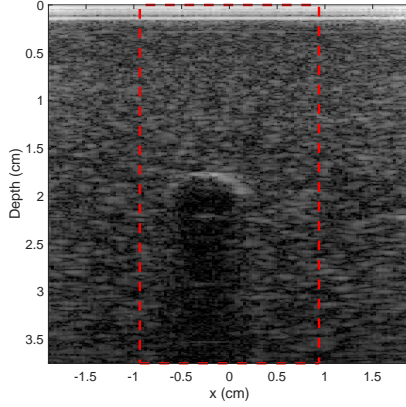
Fig. 7. Sound speed recovery maps on 16 test samples. Image (a) shows the ground truth data. Image (b) shows the sound speed maps recovered by the trained network using three plane waves and the “middle” network (see Fig 5). Gray scale values are in the range of  $1300\text{ m/s}$  (black) to  $1800\text{ m/s}$  (white).

Fig. 8. Absolute error on 16 test samples. Error has been crop at  $50\text{ m/s}$  (white). Image (a) shows the results for the reconstruction using the single central plane wave. Image (b) shows the reconstruction using three plane waves and the “middle” network (see Fig 5)

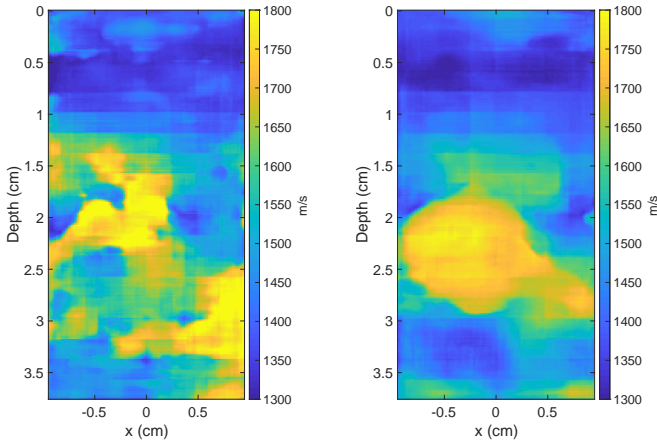
Real data require extra steps of preprocessing before feeding the data into the neural network. For the purpose of this study, we took 5 frames in each case and computed the mean values of the measurements, to reduce quantization and electronic noise. Next we applied a FIR bandpass filter to remove out of band noise. Finally, the data from the physical system contains an internal echo inside the probe that was manually cropped in addition to the excitation pulse. Effectively, this shifts the pulse zero time point from the Piezo to the probe surface.

In both cases we present the recovery results from using the single central plane wave as well as three plane waves using the “Middle” network. The single plane wave input does not convey satisfactory results for the phantom while it does work decently well with the thyroid example. Using the three plane wave, while still not as good as we would like it to be, does provide very encouraging results, showing that although more work is required, our results are definitely on the right track and convey both geometry as well sane measurements.

In the case of the polyurethane phantom, ground truth background speed of sound was measured to be  $1450\text{ m/s}$  while the speed of sound in the inclusion was measured to be roughly  $1750\text{ m/s}$ . While the size of the inclusion in the sound speed map is too big, location is correct and recovered sound speed is between  $1700\text{ m/s}$  and  $1750\text{ m/s}$ . Near the inclusion, recovered sound speed is between  $1400\text{ m/s}$  and  $1500\text{ m/s}$ , while in the near field the sound speed estimation drops too low to  $1350\text{ m/s}$ . This is actually somewhat expected at this point as our simulations are 2D and do not generate off plane speckle which is known to create a false lower velocity approximation. There is also no object in the area to help correct the assessment. Finally, speckle breaks the continuity assumption that k-wave, as well as other differential solvers, is based on, and cannot be modelled correctly in k-wave. We leave for future work, the research to find a better training model for the system, as unfortunately we are not aware of a solver that is up to the task at the moment.



(a) b-mode image



(b) sound speed - single plane wave (c) sound speed - three plane waves

Fig. 9. Reconstruction on a polyurethane phantom with an inclusion. Background sound speed has been measured at  $1450\text{ m/s}$ . Inclusion sound speed has been approximated at  $1750\text{ m/s}$ . Image (a) shows a b-mode image reconstruction from point source data. Image (b) shows the sound speed reconstruction using the single central plane wave. Image (c) shows the sound speed reconstruction using three plane waves and the “middle” network

For the thyroid image, while we do not have ground truth values, or even statistical values, to compare to. The sound speed in the muscle is within the expected range, and while not very clear, the correct structure does show up in the recovered velocity map, including the carotid artery, again giving us very encouraging real work results.

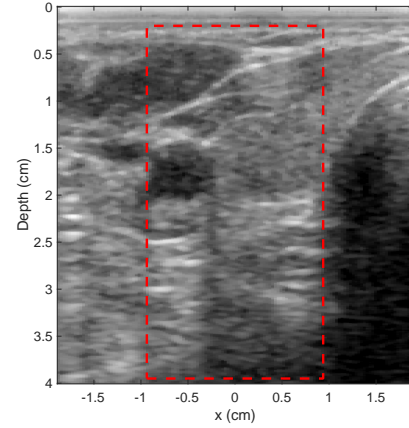
## VI. CONCLUSIONS AND FUTURE WORK

In this paper we have presented a deep learning framework for recovery of sound speed maps from plane wave ultrasound channel data. Results on synthetic data are more than an order of magnitude better than our target accuracy rate, showing that this framework has great potential for clinical purposes.

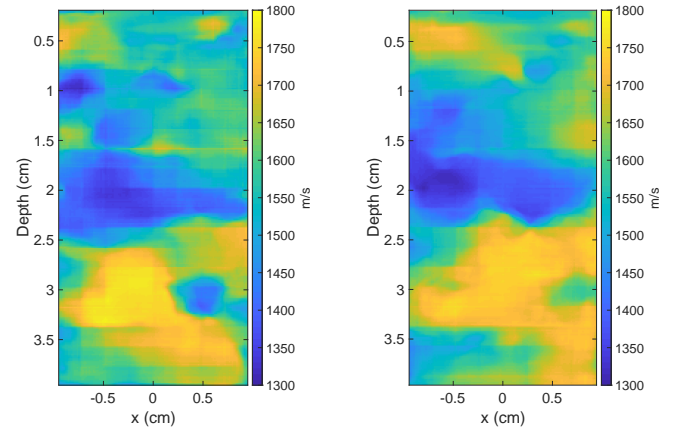
Initial real data results are also highly encouraging, although more research is required in order to improve the results, create calibrated phantoms to validate results and improve training as well as develop better simulation techniques to better train the network to deal with real data.

## REFERENCES

- [1] H. Y.-H. Lin, Y.-L. Lee, K.-D. Lin, Y.-W. Chiu, S.-J. Shin, S.-J. Hwang, H.-C. Chen, and C.-C. Hung, “Association of Renal Elasticity and Renal



(a) b-mode image



(b) sound speed - single plane wave (c) sound speed - three plane waves

Fig. 10. Reconstruction on thyroid data. Background sound speed has been measured at  $1450\text{ m/s}$ . Inclusion sound speed has been approximated at  $1750\text{ m/s}$ . Image (a) shows a b-mode image reconstruction from point source data. Image (b) shows the sound speed reconstruction using the single central plane wave. Image (c) shows the sound speed reconstruction using three plane waves and the “middle” network

Function Progression in Patients with Chronic Kidney Disease Evaluated by Real-Time Ultrasound Elastography,” *Scientific Reports*, vol. 7, Feb. 2017.

- [2] H. Singh, O. B. Panta, U. Khanal, and R. K. Ghimire, “Renal Cortical Elastography: Normal Values and Variations,” *Journal of Medical Ultrasound*, vol. 25, no. 4, pp. 215–220, Dec. 2017.
- [3] J. Carlsen, C. Ewertsen, L. Lönn, and M. Nielsen, “Strain Elastography Ultrasound: An Overview with Emphasis on Breast Cancer Diagnosis,” *Diagnostics*, vol. 3, no. 1, pp. 117–125, 2013.
- [4] J. M. Chang, J.-K. Won, K.-B. Lee, I. A. Park, A. Yi, and W. K. Moon, “Comparison of shear-wave and strain ultrasound elastography in the differentiation of benign and malignant breast lesions,” *American Journal of Roentgenology*, vol. 201, no. 2, pp. W347–W356, Aug. 2013, 00074.
- [5] R. G. Barr, G. Ferraioli, M. L. Palmeri, Z. D. Goodman, G. Garcia-Tsao, J. Rubin, B. Garra, R. P. Myers, S. R. Wilson, D. Rubens, and D. Levine, “Elastography Assessment of Liver Fibrosis: Society of Radiologists in Ultrasound Consensus Conference Statement,” *Radiology*, vol. 276, no. 3, pp. 845–861, Sep. 2015.
- [6] G. Ferraioli, P. Parekh, A. B. Levitov, and C. Filice, “Shear Wave Elastography for Evaluation of Liver Fibrosis,” *Journal of Ultrasound in Medicine*, vol. 33, no. 2, pp. 197–203, Feb. 2014.
- [7] J. F. Greenleaf, M. Fatemi, and M. Insana, “Selected methods for imaging elastic properties of biological tissues,” *Annual Review of Biomedical Engineering*, vol. 5, no. 1, pp. 57–78, Aug. 2003.
- [8] Kathy Nightingale, “Acoustic Radiation Force Impulse (ARFI) Imaging: A Review,” *Current Medical Imaging Reviews*, vol. 7, no. 4, pp. 328–

- 339, Nov. 2011.
- [9] J. L. Gennisson, T. Defieux, and M. Fink, "Ultrasound elastography: Principles and techniques," *Diagnostic and Interventional Imaging*, vol. 94, no. 5, pp. 487–495, 2013.
- [10] J. Bercoff, M. Tanter, and M. Fink, "Supersonic Shear Imaging : A New Technique for Soft Tissue Elasticity Mapping," *IEEE Transactions on Ultrasonics, Ferroelectrics and Frequency Control*, vol. 51, no. 4, pp. 396–409, 2004.
- [11] A. Nahas, M. Tanter, T.-M. Nguyen, J.-M. Chassot, M. Fink, and a. Claude Boccara, "From supersonic shear wave imaging to full-field optical coherence shear wave elastography," *Journal of biomedical optics*, vol. 18, no. 12, p. 121514, 2013.
- [12] M. S. Farvid, T. W. K. Ng, D. C. Chan, P. H. R. Barrett, and G. F. Watts, "Association of adiponectin and resistin with adipose tissue compartments, insulin resistance and dyslipidaemia," *Diabetes, Obesity and Metabolism*, vol. 7, no. 4, pp. 406–413, Jul. 2005.
- [13] J. Oudry, C. Bastard, V. Miette, R. Willinger, and L. Sandrin, "Copolymer-in-oil Phantom Materials for Elastography," *Ultrasound in Medicine and Biology*, vol. 35, no. 7, pp. 1185–1197, 2009.
- [14] C. Li, A. Stewart, and N. Duric, "Multi-grid tomographic inversion for breast ultrasound imaging," *Proceedings of SPIE*, vol. 8320, pp. 1–9, 2012.
- [15] T. Hopp, N. V. Ruiters, and N. Duric, "Breast tissue characterization by sound speed: Correlation with mammograms using a 2D/3D image registration," in *2012 IEEE International Ultrasonics Symposium*, Oct. 2012, pp. 1–4.
- [16] J. Nebeker and T. R. Nelson, "Imaging of Sound Speed Using Reflection Ultrasound Tomography," *Journal of Ultrasound in Medicine*, vol. 31, no. 9, pp. 1389–1404, Sep. 2012.
- [17] N. Duric, P. Littrup, S. Schmidt, C. Li, O. Roy, L. Bey-Knight, R. Janer, D. Kunz, X. Chen, J. Goll, A. Wallen, F. Zafar, V. Allada, E. West, I. Jovanovic, and K. Greenway, "Breast imaging with the SoftVue imaging system: First results," *Medical Imaging 2013: Ultrasonic Imaging, Tomography, and Therapy*, vol. 8675, p. 86750K, 2013.
- [18] C. Li, G. S. Sandhu, O. Roy, N. Duric, V. Allada, and S. Schmidt, "Toward a practical ultrasound waveform tomography algorithm for improving breast imaging," in *Medical Imaging 2014: Ultrasonic Imaging and Tomography*, vol. 9040, 2014, p. 90401P.
- [19] M. Sak, N. Duric, P. Littrup, L. Bey-Knight, H. Ali, P. Vallieres, M. E. Sherman, and G. L. Gierach, "Using speed of sound imaging to characterize breast density," *Ultrasound in medicine & biology*, vol. 43, no. 1, pp. 91–103, Jan. 2017.
- [20] J. R. Fincke, M. Feigin, G. A. Prieto, X. Zhang, and B. Anthony, "Towards ultrasound travel time tomography for quantifying human limb geometry and material properties," in *SPIE Medical Imaging*, N. Duric and B. Heyde, Eds., Apr. 2016, p. 97901S.
- [21] J. R. Fincke, "Imaging cortical bone using the level-set method to regularize travel-time and full waveform tomography techniques," *The Journal of the Acoustical Society of America*, vol. 141, no. 5, pp. 3549–3549, May 2017.
- [22] A. Samani, J. Zubovits, and D. Plewes, "Elastic moduli of normal and pathological human breast tissues: An inversion-technique-based investigation of 169 samples," *Physics in medicine and biology*, vol. 52, no. 6, pp. 1565–1576, 2007.
- [23] Y.-C. Fung, *Biomechanics: Mechanical Properties of Living Tissues*. New York, NY: Springer New York, 1993.
- [24] H. Hachiya, S. Ohtsuki, and M. Tanaka, "Relationship Between Speed of Sound in and Density of Normal and Diseased Rat Livers," *Japanese Journal of Applied Physics*, vol. 33, no. 5S, p. 3130, 1994.
- [25] T. Matsuhashi, N. Yamada, H. Shinzawa, and T. Takahashi, "An evaluation of hepatic ultrasound speed in injury models in rats: Correlation with tissue constituents," *Journal of Ultrasound in Medicine*, vol. 15, no. 8, pp. 563–570, Aug. 1996.
- [26] C. Li, N. Duric, P. Littrup, and L. Huang, "In vivo breast sound-speed imaging with ultrasound tomography," *Ultrasound Med Biol*, vol. 35, no. 10, pp. 1615–1628, 2009.
- [27] M. Imbault, A. Faccinnetto, B.-F. Osmani, A. Tissier, T. Defieux, J.-L. Gennisson, V. Vilgrain, and M. Tanter, "Robust sound speed estimation for ultrasound-based hepatic steatosis assessment," *Physics in Medicine and Biology*, vol. 62, no. 9, pp. 3582–3598, May 2017.
- [28] A. Benjamin, R. Zubajlo, K. Thomenius, M. Dhyani, K. Kaliannan, A. E. Samir, and B. W. Anthony, "Non-invasive diagnosis of non-alcoholic fatty liver disease (NAFLD) using ultrasound image echogenicity," in *2017 39th Annual International Conference of the IEEE Engineering in Medicine and Biology Society (EMBC)*. Seogwipo: IEEE, Jul. 2017, pp. 2920–2923.
- [29] X. Wang, Y. Peng, L. Lu, Z. Lu, M. Bagheri, and R. M. Summers, "Chestx-ray8: Hospital-scale chest x-ray database and benchmarks on weakly-supervised classification and localization of common thorax diseases," in *Computer Vision and Pattern Recognition (CVPR), 2017 IEEE Conference on*. IEEE, 2017, pp. 3462–3471.
- [30] M. F. Byrne, F. Soudan, M. Henkel, C. Oertel, N. Chapados, F. J. Echagüe, S. H. Ghalehjegh, N. Guizard, S. Giguère, M. E. MacPhail et al., "Mo1679 real-time artificial intelligence full colonoscopy workflow for automatic detection followed by optical biopsy of colorectal polyps," *Gastrointestinal Endoscopy*, vol. 87, no. 6, p. AB475, 2018.
- [31] M. Havaei, A. Davy, D. Warde-Farley, A. Biard, A. Courville, Y. Bengio, C. Pal, P.-M. Jodoin, and H. Larochelle, "Brain tumor segmentation with deep neural networks," *Medical image analysis*, vol. 35, pp. 18–31, 2017.
- [32] Y. Zhang and H. Yu, "Convolutional neural network based metal artifact reduction in x-ray computed tomography," *IEEE transactions on medical imaging*, vol. 37, no. 6, pp. 1370–1381, 2018.
- [33] Q. Yang, P. Yan, Y. Zhang, H. Yu, Y. Shi, X. Mou, M. K. Kalra, Y. Zhang, L. Sun, and G. Wang, "Low dose ct image denoising using a generative adversarial network with Wasserstein distance and perceptual loss," *IEEE transactions on medical imaging*, 2018.
- [34] E. Kang, W. Chang, J. Yoo, and J. C. Ye, "Deep convolutional framelet denoising for low-dose ct via wavelet residual network," *IEEE transactions on medical imaging*, vol. 37, no. 6, pp. 1358–1369, 2018.
- [35] Z. Zhang, X. Liang, X. Dong, Y. Xie, and G. Cao, "A sparse-view ct reconstruction method based on combination of Densenet and deconvolution," *IEEE transactions on medical imaging*, vol. 37, no. 6, pp. 1407–1417, 2018.
- [36] Y. Han and J. C. Ye, "Framing u-net via deep convolutional framelets: Application to sparse-view ct," *IEEE transactions on medical imaging*, vol. 37, no. 6, pp. 1418–1429, 2018.
- [37] X. Zheng, S. Ravishanker, Y. Long, and J. A. Fessler, "Pwls-ultra: An efficient clustering and learning-based approach for low-dose 3d ct image reconstruction," *IEEE transactions on medical imaging*, vol. 37, no. 6, pp. 1498–1510, 2018.
- [38] H. Shan, Y. Zhang, Q. Yang, U. Kruger, W. Cong, and G. Wang, "3d convolutional encoder-decoder network for low-dose ct via transfer learning from a 2d trained network," *IEEE transactions on medical imaging*, vol. 37, no. 6, pp. 1522–1534, 2018.
- [39] G. Yang, S. Yu, H. Dong, G. Slabaugh, P. L. Dragotti, X. Ye, F. Liu, S. Arridge, J. Keegan, Y. Guo et al., "Dagan: Deep de-aliasing generative adversarial networks for fast compressed sensing MRI reconstruction," *IEEE transactions on medical imaging*, vol. 37, no. 6, pp. 1310–1321, 2018.
- [40] B. Gözcü, R. K. Mahabadi, Y.-H. Li, E. Ilıcak, T. Cukur, J. Scarlett, and V. Cevher, "Learning-based compressive MRI," *IEEE transactions on medical imaging*, vol. 37, no. 6, pp. 1394–1406, 2018.
- [41] T. M. Quan, T. Nguyen-Duc, and W.-K. Jeong, "Compressed sensing MRI reconstruction using a generative adversarial network with a cyclic loss," *IEEE transactions on medical imaging*, vol. 37, no. 6, pp. 1488–1497, 2018.
- [42] B. Yang, L. Ying, and J. Tang, "Artificial neural network enhanced Bayesian PET image reconstruction," *IEEE transactions on medical imaging*, 2018.
- [43] K. Kim, D. Wu, K. Gong, J. Dutta, J. H. Kim, Y. D. Son, H. K. Kim, G. El Fakhri, and Q. Li, "Penalized PET reconstruction using deep learning prior and local linear fitting," *IEEE transactions on medical imaging*, vol. 37, no. 6, pp. 1478–1487, 2018.
- [44] A. Hauptmann, F. Lucka, M. Betcke, N. Huynh, J. Adler, B. Cox, P. Beard, S. Ourselin, and S. Arridge, "Model-based learning for accelerated, limited-view 3-d photoacoustic tomography," *IEEE transactions on medical imaging*, vol. 37, no. 6, pp. 1382–1393, 2018.
- [45] D. Allman, A. Reiter, and M. A. L. Bell, "Photoacoustic source detection and reflection artifact removal enabled by deep learning," *IEEE transactions on medical imaging*, vol. 37, no. 6, pp. 1464–1477, 2018.
- [46] A. Mousavi, G. Dasarthy, and R. G. Baraniuk, "Deepcodec: Adaptive sensing and recovery via deep convolutional neural networks," *arXiv preprint arXiv:1707.03386*, 2017.
- [47] C. A. Metzler, P. Schniter, A. Veeraraghavan, and R. G. Baraniuk, "prdeep: Robust phase retrieval with flexible deep neural networks," *arXiv preprint arXiv:1803.00212*, 2018.
- [48] S. Vedula, O. Senouf, A. M. Bronstein, O. V. Michailovich, and M. Zibulevsky, "Towards CT-quality Ultrasound Imaging using Deep Learning," *arXiv:1710.06304 [physics]*, Oct. 2017, 00000.
- [49] Y. H. Yoon, S. Khan, J. Huh, and J. C. Ye, "Efficient B-mode Ultrasound Image Reconstruction from Sub-sampled RF Data using Deep Learning," *arXiv:1712.06096 [cs, stat]*, Dec. 2017.



- [50] F. Tom and D. Sheet, "Simulating patho-realistic ultrasound images using deep generative networks with adversarial learning," in *Biomedical Imaging (ISBI 2018), 2018 IEEE 15th International Symposium on*. IEEE, 2018, pp. 1174–1177.
- [51] A. C. Luchies and B. C. Byram, "Deep Neural Networks for Ultrasound Beamforming," *IEEE Transactions on Medical Imaging*, pp. 1–1, 2018, 00005.
- [52] A. Reiter and M. A. Lediju Bell, "A machine learning approach to identifying point source locations in photoacoustic data," in *Photons Plus Ultrasound: Imaging and Sensing*, A. A. Oraevsky and L. V. Wang, Eds., Mar. 2017, p. 100643J, 00000.
- [53] H. Ravishankar, P. Sudhakar, R. Venkataramani, S. Thiruvankadam, P. Annangi, N. Babu, and V. Vaidya, "Understanding the mechanisms of deep transfer learning for medical images," in *Deep Learning and Data Labeling for Medical Applications*. Springer, 2016, pp. 188–196.
- [54] Q. Zheng, G. Tasthan, and Y. Fan, "Transfer learning for diagnosis of congenital abnormalities of the kidney and urinary tract in children based on ultrasound imaging data," in *Biomedical Imaging (ISBI 2018), 2018 IEEE 15th International Symposium on*. IEEE, 2018, pp. 1487–1490.
- [55] M. Xian, Y. Zhang, H.-D. Cheng, F. Xu, K. Huang, B. Zhang, J. Ding, C. Ning, and Y. Wang, *A Benchmark for Breast Ultrasound Image Segmentation (BUSIS)*. Infinite Study, 2018.
- [56] B. E. Treeby and B. T. Cox, "K-Wave: MATLAB toolbox for the simulation and reconstruction of photoacoustic wave fields," *Journal of Biomedical Optics*, vol. 15, no. 2, p. 021314, 2010.
- [57] B. E. Treeby, J. Jaros, D. Rohrbach, and B. T. Cox, "Modelling elastic wave propagation using the k-wave matlab toolbox," in *Ultrasonics Symposium (Ius), 2014 Ieee International*. IEEE, 2014, pp. 146–149, 00016.